

This author's accepted manuscript may be used for non-commercial purposes in accordance with [Wiley Terms and Conditions for Self-Archiving](#).

The full details of the published version of the article are as follows:

TITLE: Full-field strain of regenerated bone tissue in a femoral fracture model

AUTHORS: Aikaterina Karali, Alexander P. Kao, Richard Meeson, Marta Roldo, Gordon W. Blunn, Gianluca Tozzi

JOURNAL: Journal of Microscopy

PUBLISHER: Wiley

PUBLICATION DATE: 12 June 2020

DOI: <https://doi.org/10.1111/jmi.12937>

<PE-AT>Full-field strain of regenerated bone tissue in a femoral fracture model

Aikaterina Karali¹, Alexander P. Kao¹, Richard Meeson², Marta Roldo³, Gordon W. Blunn³, Gianluca Tozzi^{1*}

¹ Zeiss Global Centre, School of Mechanical and Design Engineering, University of Portsmouth, Portsmouth, UK

² Royal Veterinary College, Hatfield, Hertfordshire, UK

³ School of Pharmacy and Biomedical Sciences, University of Portsmouth, UK

* Correspondence: gianluca.tozzi@port.ac.uk

Abstract: The mechanical behavior of regenerated bone tissue during fracture healing is key in determining its ability to withstand physiological loads. However, the strain distribution in the newly formed tissue and how this influences the way a fracture heals it is still unclear. X-ray Computed Tomography (XCT) has been extensively used to assess the progress of mineralized tissues in regeneration and when combined with *in situ* mechanics and digital volume correlation (DVC) has been proven a powerful tool to understand the mechanical behavior and full-field three-dimensional (3D) strain distribution in bone. The purpose of this study is therefore to use *in situ* XCT mechanics and DVC to investigate the strain distribution and load-bearing capacity in a regenerating fracture in the diaphyseal bone, using a rodent femoral fracture model stabilized by external fixation. Rat femurs with 1 mm and 2 mm osteotomy gaps were tested under *in situ* XCT step-wise compression in the apparent elastic region. High strain was present in the newly formed bone (ϵ_{p1} and ϵ_{p3} reaching 29000 $\mu\epsilon$ and -43000 $\mu\epsilon$, respectively), with a wide variation and inhomogeneity of the 3D strain distribution in the regenerating tissues of the fracture gap, which is directly related to the presence of unmineralized tissue observed in histological images. The outcomes of this study will contribute in understanding natural regenerative ability of bone and its mechanical behavior under loading.

Keywords: Digital volume correlation (DVC), bone regeneration, X-ray computed tomography (XCT), *in situ* mechanics, histology

<PE-FRONTEND>

This article has been accepted for publication and undergone full peer review but has not been through the copyediting, typesetting, pagination and proofreading process, which may lead to differences between this version and the [Version of Record](#). Please cite this article as [doi: 10.1111/jmi.12937](https://doi.org/10.1111/jmi.12937).

This article is protected by copyright. All rights reserved.

1. Introduction

Bone fracture healing is a complex process that has been extensively investigated [1–5] and it is influenced by both the local biological and mechanical environment [6]. Optimal fracture healing requires mechanical stability in close proximity of the fracture ends, since large movements can negatively affect this process. However, some micromotion is necessary as completely rigid fixation has shown only partial fracture healing [1,6]. In cases where the two fracture ends are not in contact, secondary healing occurs. This can be described by three basic steps: inflammation, cellular proliferation and differentiation, and remodelling [7]. These phases occur in different locations and at different rates. In the second step, intramembranous woven bone is deposited in the void between the ends, and it is later replaced in the remodelling process by more mature lamellar bone [1]. Intramembranous and endochondral ossification can occur simultaneously leading to formation of both soft and hard callus (uncalcified and calcified/woven bone, respectively). It has been shown that hard callus starts forming in the inner layer of periosteum at a certain distance from the fracture site progressing towards the gap predominantly at the periphery [2,3], whereas soft callus is forming centrally [6]. The combination of these two actions increases the fracture stiffness and stability. Any defects that cannot heal spontaneously without intervention are considered critical-sized defects. It was recognized that defects without complete healing after 52 weeks would remain as such. In humans, non-healed defects are those induced by trauma or ablative oncological surgery [8]. A standardized method to stabilize a critical-sized defect is the use of external fixators [9–12]. They ensure alignment of the bone fragments and allow control over the degree of interfragmentary movement, which develops under external loading and muscle activity.

Histology has been widely used to assess bone healing at the microscale throughout the entire process [13,14] to identify the type of defect [15,16], to evaluate fixation efficiency [17,18] and to classify the mineralized and unmineralized tissue formation in the healing stages [13,16]. The mineralization of the fracture over time provides information on the effect of fixator stiffness [15], on the use of biomaterials and pharmaceuticals to enhance fracture healing. This investigates only selected two-dimensional (2D) regions of the tissue. Macroscopically, the fracture healing process has been also analyzed in a three-dimensional (3D) manner with the use of high-resolution X-ray computed tomography (XCT) [19–23]. Specifically, high-resolution XCT imaging allows details on the patterns of bone tissue remodeling as well as information on the time-dependent changes of bone structure during healing. However, both 2D and 3D imaging evaluations were only able so far to quantify the morphology of bone regeneration, without any specific information on its quality in terms of mechanical properties.

Digital volume correlation (DVC) is gaining increased popularity in the experimental computation of 3D full-field strain in bone. Typically, DVC correlates high-resolution XCT images obtained *in situ* to measure the full-field displacement and derived strain at the tissue [24,25] and bone apparent levels [26–28]. DVC has been used on long bones to better understand the strain distribution of *in vivo* experiments on mice tibia [29], where the tibiae were tested within an *in vivo* XCT system and DVC performed on these tomograms to identify the precision error of local strains. Additionally, DVC was employed to compute the full-field strain at tissue level in bone specimens where the newly formed bone was favored by the action of resorbable biomaterials [30,31]. Digital image correlation (DIC) has also been applied to identify the 2D strains on the surface of intact whole bone [32]. To such extent, Yavari et al. (2013) used DIC to examine 3D surface strains in the linear elastic region of rat

femora during compression testing until failure, in order to elaborate strain-based fracture criteria [33].

To the best of the authors' knowledge, the investigation of internal strain distribution in the regenerated bone of naturally healed fracture models using DVC has not been previously investigated. Therefore, the aim of this study is to assess the load-bearing capacity and the 3D full-field strain distribution in the regenerated diaphyseal bone tissue using DVC. Furthermore, histology is used to assess the regeneration status of both calcified and uncalcified tissues in the region.

2. Materials and Methods

2.1 Materials

Seven Wistar rat female femurs with osteotomy in the diaphysis of 1 mm and 2 mm gap (S1-S4 and S5-S6, respectively) were used in this study. The gap was stabilised with a Stanmore Micro-External-Fixator (SMExF) [18]. The animals were sacrificed 5 weeks postoperative and the femurs were extracted and fixed in formalin solution (10% buffered formaldehyde). Both ends were embedded in Poly(methyl methacrylate) (PMMA) and Acetyl endcaps [34]. The average height of the femurs was 38 ± 2.3 mm; consequently, the tissue in between the endcaps was 20 ± 2.3 mm. The fixator was removed prior to the *in situ* mechanical testing.

2.2 High-resolution XCT imaging

High-resolution XCT was performed using a Versa 510 system (Carl Zeiss Microscopy, USA). The system operated at 110V/9kW and 1601 projections were collected on air using a 0.4x objective with exposure time of 3 seconds over 360° , resulting in a $12 \mu\text{m}$ voxel size. The resulting field of view (FOV) included the osteotomy gap and the 2 closest pin holes (12×12 mm).

2.3 *In situ* XCT mechanics

In order to plan the *in situ* XCT experiments with incremental increases of compressive load, a preliminary test was conducted in order to document damage induced by fixator removal as well as defining the apparent elastic region extension to be used as a reference for the step-wise XCT mechanics. One femur with a 1 mm osteotomy gap (S1) was XCT imaged before and after removal of the fixator, then uniaxially compressed *in situ* with a loading device (CT5000, Deben, UK) until failure and finally XCT imaged post-failure. It was shown that removal of the fixator did not cause any visible damage to this specimen (Fig.1A) and failure occurred at ~ 1.2 mm displacement (Fig.1B, C).

Figure 1

For the *in situ* step-wise compression testing the bone was kept hydrated throughout the process by wrapping the tissue with a gauze immersed in saline solution and then in a paraffin film to avoid leakage. The distal end of the femur was fixed to the bottom plate. An initial pre-load of 7 ± 2.7 N was applied and two consecutive tomograms were acquired to calculate DVC strain uncertainties (zero-

strain test [26]). The specimens were then step-wise compressed to 0.5 mm and 1 mm displacements, as dictated by the preliminary experiment, within their apparent elastic region. Following the application of each displacement step, the specimens were allowed to relax for 15 min, to compensate for stress relaxation, before acquiring XCT images [35].

2.4 Image post-processing

The 3D datasets obtained from the tomograms after reconstruction (1004x1024 pixels, 32-bit) were converted to 8-bit and rigidly registered using FIJI (ImageJ, USA). Parallelepipeds were cropped in the centre of the dataset ensuring that the osteotomy and one of the pin holes were in the region of interest (ROI) (Figs. 3 and 4). Non-bone voxels in the images were given a zero-intensity value in the grey-scale by applying a mask to each dataset [36]. The mask was created by running a purifying cycle on the binary image of each dataset with BoneJ plug-in. An arithmetic and logical operation was executed between the original dataset and the purified images to remove the noise using the same software [37].

2.5 Digital Volume Correlation

A local approach DVC analysis was performed for the cropped volumes (Fig.2, Fig.3) using DaVis 10.0.3 (LaVision, UK). A multi-step processing scheme (128 to 48 voxels/subvolume) was used to compute the strain, followed by a vector post-processing, where the correlation coefficient was thresholded to 0.8. The first two consecutive datasets where the pre-load was applied were used for the calculation of the strain error uncertainty (<300 $\mu\epsilon$ in all cases) [27,38,39]. The 1st and 3rd principal (ϵ_{p1} and ϵ_{p3}) strains were then computed.

2.6 Histological analysis

After *in situ* testing the specimens were decalcified in formic acid, dehydrated in increasing concentration of ethanol (50%, 75%, 85%, 95%, 100%) and cleared in xylene (C8H10). Then, they were infiltrated with paraffin wax for 30 hours positioned in the same plane with the pin holes oriented vertically and embedded in wax. Sections of 5 μm were cut from the middle of each specimen using Leica RM2235 rotary microtome (Leica Biosystems, UK) [18] and mounted on glass slides. The paraffin wax was removed and sections stained using Haematoxylin & Eosin (H&E) [40,41]. The osteotomy gap region was located under 10x magnification lens and the tissue was analysed at 50x magnification using Olympus BX40 (Leica Biosystems, UK). The soft (i.e. cartilaginous matrix, skin, muscles, fibrous) and hard (i.e. cortical, woven bone) tissue were identified in the periosteal, intracortical and intramedullary zones.

3. Results

The XTC images showed differences in the morphology of the regenerated mineralized tissue. Only S1 showed complete healing after 5 weeks (Fig.1A). In S2, S3, S4 (1 mm gap, Fig.2A-C) and S5 (2 mm gap, Fig.3A) partial healing was shown, whereas S6 (Fig.3B) formed a non-union.

Figure 2

Figure 3

The strain induced on the regenerated tissue throughout the compression steps was assessed using DVC. In S2-S5 (Figs. 4A-C and 5A) an overall buckling of the structure was observed. The 1st principal strain (ϵ_{p1}) showed a wide variation of the strain concentration. S2 experienced higher strain level in the borders of the specimen where there was lack of woven bone (maximum $\approx 29000 \mu\epsilon$) (Fig.4I, II A). Conversely, in S3 and S4 strain concentration was present in the woven bone (exceeding $20000 \mu\epsilon$) (Fig.4I, II B and C). Due to their morphology, the femurs with a 2 mm osteotomy gap showed different strain distributions. S5 exhibited an increase in the strain inferiorly, not exceeding $15000 \mu\epsilon$ (Fig.5I, II A). The results for S6 were different from the rest, since the XCT images were unable to resolve callus bridging the osteotomy region. For this specimen the DVC analysis showed higher strain levels on the surface of the proximal fracture end (maximum $\approx 18000 \mu\epsilon$) (Fig.5I, II B). As for ϵ_{p3} , in S2 (Fig.4III, IV A) compressive strains were accumulated laterally ($\approx -30000 \mu\epsilon$) in the first compression step; prompting contact between the two fracture ends at the second compression step, where the volume of the tissue under compression increased, not exceeding $-32000 \mu\epsilon$. The load in S3 was primarily maintained by the woven bone ($\approx -2000 \mu\epsilon$) at $\Delta L = 0.5$ mm and inducing compressive strains locally in regions with less hard tissue formation ($\approx -28000 \mu\epsilon$) (Fig.4III B). At $\Delta L = 1.0$ mm, ϵ_{p3} in S3 resulted in similar trends as before; however, the strain induced in the woven bone reached a value of $-5000 \mu\epsilon$ (Fig.4IV B). The strain distribution in S4 was similar throughout its volume ranging between $-1000 \mu\epsilon$ and $-4000 \mu\epsilon$ after the first compression step (Fig.4III C). The hard callus peripherally of the periosteum sustained the load, reaching $-43000 \mu\epsilon$ locally in the second compression step (Fig.4IV C). S3 and S4 displayed lower strain levels compared to S2 in the first compression step (Fig.4I, III). Specifically, lower strain was distributed when woven bone was present in either side of the gap, maintaining a stable mechanical environment. The callus formation in S4 supported the compressive load at $\Delta L = 1.0$ mm without signs of buckling and concentration of compressive strain experienced on both sides of the fracture (Fig.4IV C). In S5 (Fig.5III, IV A), the strain was concentrated in the middle of the woven bone locally in the first compression step, spreading laterally in the regenerated tissue on the second step. The behavior of S6 (Fig. 5III, IV B) is different compared to S5; since the compression induced a sliding-like effect on the two parts of the fracture. The strain in the woven bone laterally showed an increase in magnitude of $10000 \mu\epsilon$ going from $\approx -20000 \mu\epsilon$ to $\approx -30000 \mu\epsilon$ (Fig.5III, IV B).

Figure 4

Figure 5

Histological results from S2, S3 (Fig.6), S4 and S5, showed the osteotomy gap undergoing fracture healing. Both hard and soft callus formation was evident in the same fracture with mineralization of the tissue being dominant laterally. In the higher magnification images, endochondral ossification

was observed, leading to the formation of disorganized woven bone that formed an external callus on the surfaces of the cortical bone (Fig.6). Cartilage matrix was observed within the osteotomy gaps, with mineralized chondrocytes. The histology in S4 also showed evidence of fibrous tissue intercortically. S6 was classified as a non-union based on the histology (Fig.7). Woven bone was found to be present at the surface of the both fracture ends, along with the cartilage matrix in the middle of the osteotomy gap. However, there was no bridging between the two.

Figure 6

Figure 7

4. Discussion

In this study XCT images showed that how fracture healing status differed in all six specimens, having complete (S1, Fig.1) and partial (S2-S4, Fig.2 and S5, Fig.3A) healing, as well as non-union (S6, Fig.3B). In general, tissue formation patterns throughout the healing process are highly depended on the duration, gap size and quality of the fixation [18,42–44]. The consequent variation in tissue formation affected the strain distribution under the two displacement conditions. It has been shown that the intermittent tissue calcification during endochondral ossification and continuing growth of callus volume, increased the fracture stiffness and stability [6]. Here, not only there were differences in strain between the 1 and 2 mm groups, but also high variability in the strain distribution within a single fracture and this explains how tissue formation in the fracture gap was not uniform. This was associated with variation of the tissue strain in the osteotomy gap. In the 1 mm osteotomy gap specimens (Fig. 4) at $\Delta L = 0.5$ mm, S2 exhibited high strain laterally. Compressive strain ($\approx -30000 \mu\epsilon$) appeared in the area with visually higher levels of hard callus formation. Interestingly from the histology images, it was seen that area under tension is filled with cartilage matrix and mineralized chondrocytes (Fig. 6). This was promoted by an unstable *in vivo* mechanical environment, where the woven bone sustained the compression causing the cartilage matrix to tension [ϵ_{p1} exceeding $20000 \mu\epsilon$ locally (Figs. 4I, II and 5I, II)].

The difference in the mechanical behavior of S3 and S4 to S2 is better understood from the histology images. S3 illustrates an even distribution of soft and hard callus formation in the osteotomy gap (Fig. 6), with soft callus formation and advanced endochondral ossification where the cartilage matrix mineralized into woven bone. The combination of the two provided the mechanical support in the overall structure under loading [2,45]. However, the fact that endochondral ossification was more dominant on one side instigated a buckling effect. In the case of S4 the XCT images showed high levels of woven bone formation extra- and intracortically and it could be assumed that bone was at the beginning of the remodelling stage in the fracture healing (Fig. 2) [19]. Only a small region presented no hard callus formation. The histology images of that area showed presence of fibrous tissue along with osteoblasts in close proximity. S5 showed increased levels of compressive strain localized at the intra-cortical callus in the first compression step, which extended towards the rest of the callus as well as the cortex of the fracture ends in the second step. In this case of 2 mm osteotomy gap, union has formed, providing interfragmentary mechanical stability [2]. The

histological analysis showed the presence of cartilage matrix in that area that helped load transfer in these regions [46]. Although the peak value of strain is decreased at $\Delta L = 1.0$ mm, the volume under higher compressive strain levels increased, thus maintaining the higher load. The last specimen S6 was a clear case of non-union. The load was conveyed between the two fracture ends through contact and sustained by the skin and muscles surrounding the bone. This assumption is made through observation of the specimen status post-XCT imaging and histological analysis (Figs. 3B and 7). By contact, the fracture ends of the specimen appeared to be more flexible than the rest and visually there was no tearing of the skin surrounding the bone. From the histological images, endochondral ossification was detected; however, there was no bridging and both ends were surrounded by cartilage matrix. The sliding-like effect of the compressive load deformed the interfracture mineralized tissue reaching $\approx -30000 \mu\epsilon$ locally (Fig. 5IV B).

Controls were not available for comparison of the mechanics in intact and whole bone during fracture healing. However, the strain induced via compression on healthy young and mature rat femurs has been previously measured using DIC on the surface on the diaphysis [33]. The full-field measurements before failure displayed high levels of strain in the diaphysis reaching $\approx -11000 \mu\epsilon$ in the younger specimens and $\approx -17000 \mu\epsilon$ in the mature ones. Furthermore, full-field strain distribution using DVC in long bones under physiological loading conditions (not exceeding 13 N of total load) exhibited higher strain in the proximal and distal end of the bone [29]. Specifically, the highest and lowest ϵ_{p3} values in the mid-shaft region in all the specimens reached -17000 ± 2390 and $-7504 \pm 4347 \mu\epsilon$. In the current study, strains obtained for the fracture site at the first compression step in S4 were one order of magnitude lower than the ones presented in both these studies [29,33]. Overall, the specimens with 1 mm osteotomy gap, only locally in the extra-cortical woven bone exhibited higher values of strain ($\approx -30000 \mu\epsilon$) than that mentioned in Giorgi and Dall'Ara (2018) [29]. The full-field strain measurements in the second group displayed higher compressive values ($\approx -43000 \mu\epsilon$), which can be attributed to the larger osteotomy gap and therefore axial volume of woven bone. 3D full-field strain concentration in regenerated tissue has been examined in cylindrical trabecular bone specimens that included osteoregenerative grafts [30,31]. DVC analysis was performed in regions which included the interface between the native bone tissue and grafts. In the case of this study there are no biomaterials introduced to the structure; however, a correlation can be made in the strain values of regenerated tissue between the two studies. The specimen with the largest amount of new bone formation displaced higher compressive strain levels in the regenerated tissue compared to bone graft reaching a maximum of $-15000 \mu\epsilon$ [30]. Similarly, in Peña- Fernández et al. (2020) the DVC analysis showed that the newly formed bone experienced the highest strain values in the specimen of $\approx -10000 \mu\epsilon$ [31].

The mechanical behavior of the soft tissue (i.e. cartilage matrix, muscles and skin) in the fracture site cannot be easily quantified by XCT-based evaluations, due to their low absorption. The cartilage matrix, where endochondral ossification occurred, should have experienced similar deformation as the woven bone around it. However, in areas of intramembranous ossification the strain in the adjacent soft tissues was unknown. Characterization of the mechanical properties of the callus formed via intramembranous ossification is vital in the understanding of factors determining healing process and mechanical stability [22]. This could be potentially achieved by using *in situ* mechanics with an optimized combination of tissue staining and XCT phase-contrast, which would provide DVC with sufficient pattern to enable correlation in soft-hard tissue interfaces [47].

This study has a number of limitations. A limited number of specimens for both 1 mm and 2 mm osteotomy gaps were available and the *ex vivo* analysis is representative of a single time point during the healing processes. The main interest of this study was in understanding the load transferred through the osteotomy gap and the associated strain levels; for that reason, the bone was loaded after removal of the external fixator. In future, the strain pattern in the osteotomy gap with the fixator still in position can be investigated, as this will give a real value of the strain in the tissues during the healing process. Nevertheless, the differences observed in the local strain distribution for both 1 mm and 2 mm osteotomy gaps were related to the level of bone formation *in vivo*. It could be argued that mechanics of the tissue may be altered by the fixation process, but it has been shown that fixation should not alter the apparent elastic properties of bone [48]. In any case, the methodology reported in this study provide a valuable guideline for XCT-based analysis of regenerated fractures and can be used to inform/validate computational models predicting bone regeneration mechanism.

5. Conclusion

This study presented an approach to evaluate the 3D full-field strain distribution using DVC, within the regenerated bone tissue of two different osteotomy gaps in the diaphysis of rat femurs, induced by *in situ* XCT step-wise compression loading in the apparent elastic region. The regenerated mineralized tissue was evaluated via high-resolution XCT imaging and the soft callus formation was examined through histology. All specimens were at a different stage of healing leading to variability in the strain values under loading. The histological analysis showed endochondral ossification in all the specimens, except one where a non-union had occurred. Overall, it was observed that in the specimens with partial regeneration, the newly formed bone experienced high strain (ϵ_{p1} between 18000 $\mu\epsilon$ and 29000 $\mu\epsilon$; ϵ_{p3} between -30000 $\mu\epsilon$ and -43000 $\mu\epsilon$). In the case of non-union the strain reached -30000 $\mu\epsilon$ (ϵ_{p3}) and the cartilaginous and soft tissues in the region of the osteotomy gap sustained strain reaching 18000 $\mu\epsilon$ (ϵ_{p1}).

Acknowledgments

The authors gratefully acknowledge Dr Robin Rumney, Ms Lowrie Vayro, Ms Amanda Chase and Ms Julie Rogers (School of Pharmacy and Biomedical Sciences, University of Portsmouth) for their assistance in the histology protocol, Mr Geoff Britton and Mr Robert Elliot (School of Mechanical and Design Engineering, University of Portsmouth) for their help with the experimental set up. The Zeiss Global Centre (University of Portsmouth) provided XCT imaging and DVC capability to conduct this study. This research was partially funded by the Medical Research Council (grant no., UK: MR/N002318/1). This study is part of a PhD programme funded by the Faculty of Technology (University of Portsmouth).

References

- [1] S.M. Perren, Physical and biological aspects of fracture healing with special reference to internal fixation, *Clin. Orthop. Relat. Res.* (1979) 175–196.
http://journals.lww.com/corr/Citation/1979/01000/Physical_and_Biological_Aspects_of_Fracture.27.aspx.
- [2] F. Loi, L.A. Córdova, J. Pajarinen, T. Hua Lin, Z. Yao, S.B. Goodman, Inflammation, fracture and bone repair, *Bone*. 86 (2016) 119–130. doi:10.1016/j.bone.2016.02.020.
- [3] L. Claes, S. Recknagel, A. Ignatius, Fracture healing under healthy and inflammatory conditions, *Nat. Rev. Rheumatol.* 8 (2012) 133–143. doi:10.1038/nrrheum.2012.1.
- [4] Z. Zhao, D. Yang, X. Ma, H. Zhao, C. Nie, Z. Si, Successful Repair of a Critical-Sized Bone Defect in the Rat Femur with a Newly Developed External Fixator, *Tohoku J. Exp. Med.* 219 (2009) 115–120. doi:10.1620/tjem.219.115.
- [5] B. McKibbin, The biology of fracture healing in long bones, *J. Bone Jt. Surg.* 60-B (1978) 150–162. doi:10.1007/978-1-4471-5451-8_139.
- [6] P.J. Harwood, J.B. Newman, A.L.R. Michael, (ii) An update on fracture healing and non-union, *Orthop. Trauma*. 24 (2010) 9–23. doi:10.1016/j.mporth.2009.12.004.
- [7] R. Marsell, T.A. Einhorn, The biology of fracture healing, *Injury*. 42 (2011) 551–555. doi:10.1016/j.injury.2011.03.031.
- [8] S. Ochandiano Caicoya, Bone cavity filling with alloplastic material in maxillofacial surgery, *Rev Esp Cir Oral y Maxilofac.* 1 (2007) 21–32. doi:10.4321/S1130-05582007000100003.
- [9] L. Claes, R. Grass, T. Schmickal, B. Kisse, C. Eggers, H. Gerngroß, W. Mutschler, M. Arand, T. Wintermeyer, A. Wentzensen, Monitoring and healing analysis of 100 tibial shaft fractures, *Langenbeck's Arch. Surg.* 387 (2002) 146–152. doi:10.1007/s00423-002-0306-x.
- [10] S.J. Kaplan, W.C. Hayes, P. Mudan, J.L. Lelli, A.A. White, Monitoring the healing of a tibial osteotomy in the rabbit treated with external fixation, *J. Orthop. Res.* 3 (1985) 325–330. doi:10.1002/jor.1100030309.
- [11] F.G. Lippert, C. Hirsch, The three dimensional measurement of tibia fracture motion by photogrammetry, *Clin. Orthop. Relat. Res.* 105 (1974) 130–143.
- [12] K. Seide, N. Weinrich, M.E. Wenzl, D. Wolter, C. Jürgens, Three-dimensional load measurements in an external fixator, *J. Biomech.* 37 (2004) 1361–1369. doi:10.1016/j.jbiomech.2003.12.025.
- [13] I. Manjubala, Y. Liu, D.R. Epari, P. Roschger, H. Schell, P. Fratzl, G.N. Duda, Spatial and temporal variations of mechanical properties and mineral content of the external callus during bone healing, *Bone*. 45 (2009) 185–192. doi:10.1016/j.bone.2009.04.249.
- [14] J. Mora-Macías, A. Pajares, P. Miranda, J. Domínguez, E. Reina-Romo, Mechanical characterization via nanoindentation of the woven bone developed during bone transport, *J. Mech. Behav. Biomed. Mater.* 74 (2017) 236–244. doi:10.1016/j.jmbbm.2017.05.031.
- [15] M. Zandi, A. Dehghan, F. Gheysari, L. Rezaeian, N. Mohammad Gholi Mezerji, Histological

- evaluation of the healing process of autografted mandibular bone defects in rats under treatment with zoledronate, *European Association for Cranio-Maxillo-Facial Surgery*, 2019. doi:10.1016/j.jcms.2018.11.015.
- [16] D.R. Epari, H. Schell, H.J. Bail, G.N. Duda, Instability prolongs the chondral phase during bone healing in sheep, *Bone*. 38 (2006) 864–870. doi:10.1016/j.bone.2005.10.023.
- [17] L. Claes, P. Augat, S. Schorlemmer, C. Konrads, A. Ignatius, C. Ehrnthaller, Temporary distraction and compression of a diaphyseal osteotomy accelerates bone healing, *J. Orthop. Res.* 26 (2008) 772–777. doi:10.1002/jor.20588.
- [18] R. Meeson, M. Moazen, A. Sanghani-Kerai, L. Osagie-Clouard, M. Coathup, G. Blunn, The influence of gap size on the development of fracture union with a micro external fixator, *J. Mech. Behav. Biomed. Mater.* 99 (2019) 161–168. doi:10.1016/j.jmbbm.2019.07.015.
- [19] H. Isaksson, I. Gröngröft, W. Wilson, C.C. Van Donkelaar, B. Ven Rietbergen, A. Tami, R. Huiskes, K. Ito, Remodeling of fracture callus in mice is consistent with mechanical loading and bone remodeling theory, *J. Orthop. Res.* 27 (2009) 664–672. doi:10.1002/jor.20725.
- [20] E.F. Morgan, Z.D. Mason, K.B. Chien, A.J. Pfeiffer, G.L. Barnes, T.A. Einhorn, L.C. Gerstenfeld, Micro-computed tomography assessment of fracture healing: Relationships among callus structure, composition, and mechanical function, *Bone*. 44 (2009) 335–344. doi:10.1016/j.bone.2008.10.039.
- [21] T. Kustro, T. Kiss, D. Chernohorskyi, Y. Chepurnyi, Z. Helyes, A. Kopchak, Quantification of the mandibular defect healing by micro-CT morphometric analysis in rats, *J. Cranio-Maxillofacial Surg.* 46 (2018) 2203–2213. doi:10.1016/j.jcms.2018.09.022.
- [22] S.J. Shefelbine, U. Simon, L. Claes, A. Gold, Y. Gabet, I. Bab, R. Müller, P. Augat, Prediction of fracture callus mechanical properties using micro-CT images and voxel-based finite element analysis, *Bone*. 36 (2005) 480–488. doi:10.1016/j.bone.2004.11.007.
- [23] Y. Gabet, R. Müller, E. Regev, J. Sela, A. Shteyer, K. Salisbury, M. Chorev, I. Bab, Osteogenic growth peptide modulates fracture callus structural and mechanical properties, *Bone*. 35 (2004) 65–73. doi:10.1016/j.bone.2004.03.025.
- [24] F. Gillard, R. Boardman, M. Mavrogordato, D. Hollis, I. Sinclair, F. Pierron, M. Browne, The application of digital volume correlation (DVC) to study the microstructural behaviour of trabecular bone during compression, *J. Mech. Behav. Biomed. Mater.* 29 (2014) 480–499. doi:10.1016/j.jmbbm.2013.09.014.
- [25] M. Peña-Fernández, S. Cipiccia, E. Dall’Ara, A.J. Bodey, R. Parwani, M. Pani, G.W. Blunn, A.H. Barber, G. Tozzi, Effect of SR-microCT radiation on the mechanical integrity of trabecular bone using in situ mechanical testing and digital volume correlation., *J. Mech. Behav. Biomed. Mater.* 88 (2018) 109–119. doi:10.1016/j.jmbbm.2018.08.012.
- [26] E. Dall’Ara, M. Peña-Fernández, M. Palanca, M. Giorgi, L. Cristofolini, G. Tozzi, Precision of Digital Volume Correlation Approaches for Strain Analysis in Bone Imaged with Micro-Computed Tomography at Different Dimensional Levels, *Front. Mater.* 4 (2017). doi:10.3389/fmats.2017.00031.
- [27] G. Tozzi, V. Danesi, M. Palanca, L. Cristofolini, Elastic Full-Field Strain Analysis and

- Microdamage Progression in the Vertebral Body from Digital Volume Correlation, *Strain*. 52 (2016) 446–455. doi:10.1111/str.12202.
- [28] D. Christen, A. Levchuk, S. Schori, P. Schneider, S.K. Boyd, R. Müller, Deformable image registration and 3D strain mapping for the quantitative assessment of cortical bone microdamage, *J. Mech. Behav. Biomed. Mater.* 8 (2012) 184–193. doi:10.1016/j.jmbbm.2011.12.009.
- [29] M. Giorgi, E. Dall’Ara, Variability in strain distribution in the mice tibia loading model: A preliminary study using digital volume correlation, *Med. Eng. Phys.* 62 (2018) 7–16. doi:10.1016/j.medengphy.2018.09.001.
- [30] M. Peña Fernández, E. Dall’Ara, A.J. Bodey, R. Parwani, A.H. Barber, G.W. Blunn, G. Tozzi, Full-Field Strain Analysis of Bone-Biomaterial Systems Produced by the Implantation of Osteoregenerative Biomaterials in an Ovine Model, *ACS Biomater. Sci. Eng.* 5 (2019) 2543–2554. doi:10.1021/acsbomaterials.8b01044.
- [31] M. Peña-Fernández, C. Black, J. Dawson, D. Gibbs, J. Kanczler, R.O.C. Oreffo, G. Tozzi, Exploratory Full-Field Strain Analysis of Regenerated Bone Tissue from Osteoinductive Biomaterials, *Materials (Basel)*. 13 (2020) 1–16. doi:doi:10.3390/ma13010168.
- [32] P. Sztrefek, M. Vanleene, R. Olsson, R. Collinson, A.A. Pitsillides, S. Shefelbine, Using digital image correlation to determine bone surface strains during loading and after adaptation of the mouse tibia, *J. Biomech.* 43 (2010) 599–605. doi:10.1016/j.jbiomech.2009.10.042.
- [33] S.A. Yavari, J. van der Stok, H. Weinans, A.A. Zadpoor, Full-field strain measurement and fracture analysis of rat femora in compression test, *J. Biomech.* 46 (2013) 1282–1292. doi:10.1016/j.jbiomech.2013.02.007.
- [34] T.M. Keaveny, X.E. Guo, T.A. McMahon, E.F. Wachtel, W.C. Hayes, Trabecular bone exhibits fully linear elastic behavior and yields at low strains, *J. Biomech.* 27 (2004) 1127–1136. doi:10.1016/0021-9290(94)90053-1.
- [35] K. Madi, G. Tozzi, Q.H. Zhang, J. Tong, A. Cossey, A. Au, D. Hollis, F. Hild, Computation of full-field displacements in a scaffold implant using digital volume correlation and finite element analysis, *Med. Eng. Phys.* 35 (2013) 1298–1312. doi:10.1016/j.medengphy.2013.02.001.
- [36] M. Peña-Fernández, A.H. Barber, G.W. Blunn, G. Tozzi, Optimization of digital volume correlation computation in SR-microCT images of trabecular bone and bone-biomaterial systems, *J. Microsc.* 272 (2018) 213–228. doi:10.1111/jmi.12745.
- [37] M. Doube, M.M. Klosowski, I. Arganda-Carreras, F.P. Cordelières, R.P. Dougherty, J.S. Jackson, B. Schmid, J.R. Hutchinson, S.J. Shefelbine, BoneJ: Free and extensible bone image analysis in ImageJ, *Bone*. 47 (2010) 1076–1079. doi:10.1016/j.bone.2010.08.023.
- [38] M. Palanca, A.J. Bodey, M. Giorgi, M. Viceconti, D. Lacroix, L. Cristofolini, E. Dall’Ara, Local displacement and strain uncertainties in different bone types by digital volume correlation of synchrotron microtomograms, *J. Biomech.* 58 (2017) 27–36. doi:10.1016/j.jbiomech.2017.04.007.
- [39] M. Palanca, G. Tozzi, L. Cristofolini, M. Viceconti, E. Dall’Ara, Three-Dimensional Local Measurements of Bone Strain and Displacement: Comparison of Three Digital Volume

- Correlation Approaches, *J. Biomech. Eng.* 137 (2015) 071006. doi:10.1115/1.4030174.
- [40] L.C. Junqueira, J. Carneiro, *Basic Histology text & atlas*, 11th ed., McGraw-Hill companies, 2005.
- [41] M.H. Ross, P. Wojciech, *Histology a Text and Atlas With correlated cell and molecular biology*, 5th ed., LIPPINCOTT WILLIAMS & WILKINS, Baltimore, 2006.
- [42] A. Vetter, D.R. Epari, R. Seidel, H. Schell, P. Fratzl, G.N. Duda, R. Weinkamer, Temporal tissue patterns in bone healing of sheep, *J. Orthop. Res.* 28 (2010) 1440–1447. doi:10.1002/jor.21175.
- [43] M.J. Gómez-Benito, J.M. García-Aznar, J.H. Kuiper, M. Doblaré, Influence of fracture gap size on the pattern of long bone healing: A computational study, *J. Theor. Biol.* 235 (2005) 105–119. doi:10.1016/j.jtbi.2004.12.023.
- [44] D.C. Betts, E. Wehrle, G.R. Paul, G.A. Kuhn, P. Christen, S. Hofmann, R. Muller, The association between mineralised tissue formation and the mechanical local in vivo environment : Time-lapsed quantification of a mouse defect healing model, *Sci. Rep.* (2020) 1–10. doi:http://dx.doi.org/10.1101/721365.
- [45] T.E. Jørgensen, Measurements of stability of crural fractures treated with hoffmann osteotaxis: 2.measurements on crural fractures, *Acta Orthop.* 43 (1972) 207–218. doi:10.3109/17453677208991258.
- [46] M.S. Ghiasi, J. Chen, A. Vaziri, E.K. Rodriguez, A. Nazarian, Bone fracture healing in mechanobiological modeling: A review of principles and methods, *Bone Reports.* 6 (2017) 87–100. doi:10.1016/j.bonr.2017.03.002.
- [47] J.N. Clark, A. Garbout, S.A. Ferreira, B. Javaheri, A.A. Pitsillides, S.M. Rankin, J.R.T. Jeffers, U. Hansen, Propagation phase-contrast micro-computed tomography allows laboratory-based three-dimensional imaging of articular cartilage down to the cellular level, *Osteoarthr. Cartil.* 28 (2020) 102–111. doi:10.1016/j.joca.2019.10.007.
- [48] J. Wieding, E. Mick, A. Wree, R. Bader, Influence of three different preservative techniques on the mechanical properties of the ovine cortical bone, *Acta Bioeng. Biomech.* 17 (2015) 137–146. doi:10.5277/ABB-00067-2014-03.

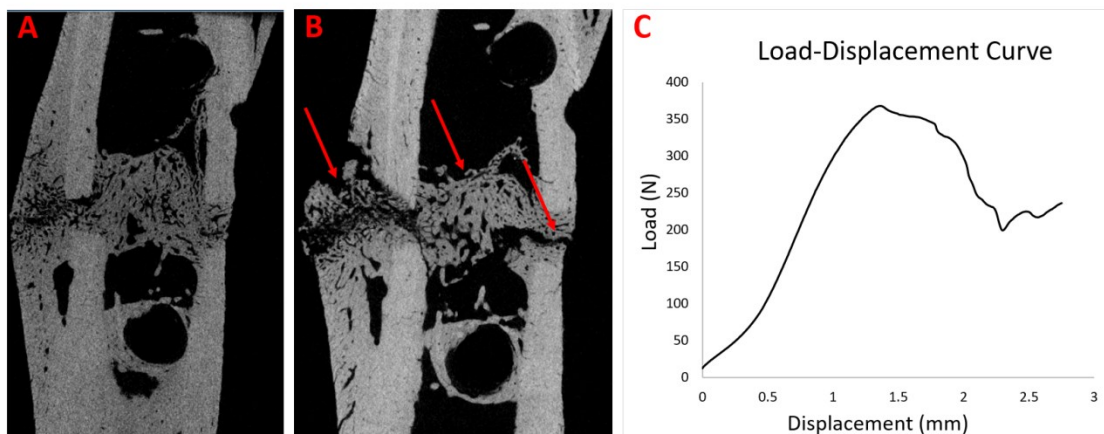


Figure 1. XCT tomograms of S1 before (A) and after (B) compression until failure, where red arrows are indicating cracks forming in the regenerated bone tissue. The entire load-displacement curve for the specimen is also shown (C).

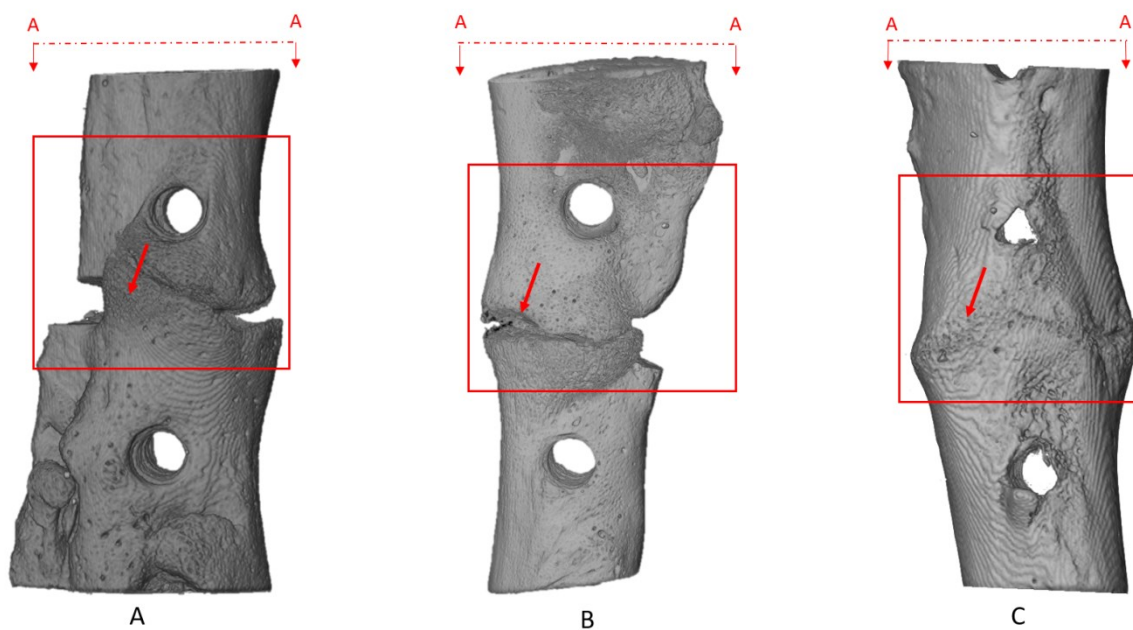


Figure 2. XCT images of rat femurs with 1 mm osteotomy gap (red arrow) under a 7 ± 2.7 N pre-load. The red square is outlining the ROIs of S2 (A), S3 (B) and S4 (C) cropped during the image post-processing.

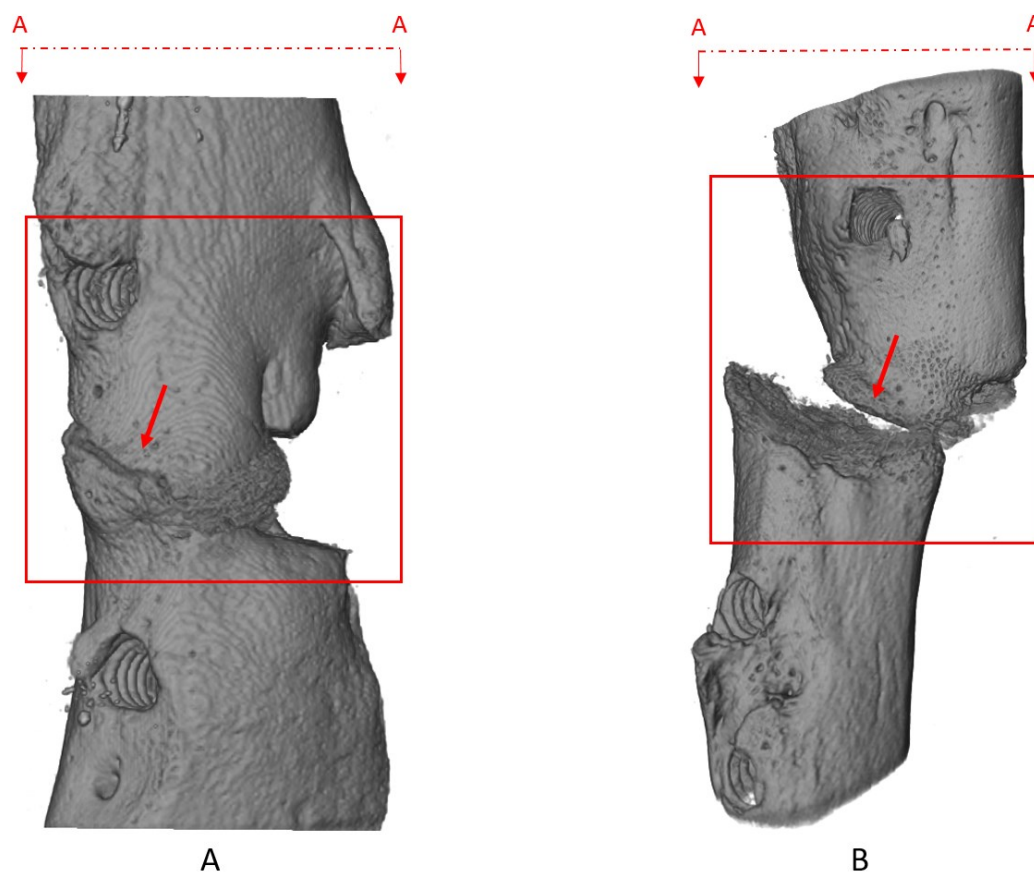


Figure 3. XCT images of rat femurs with 2 mm osteotomy gap (red arrow) under a 7 ± 2.7 N pre-load. The red square is outlining the ROIs of S5 (A) and S6 (B) cropped during the image post-processing.

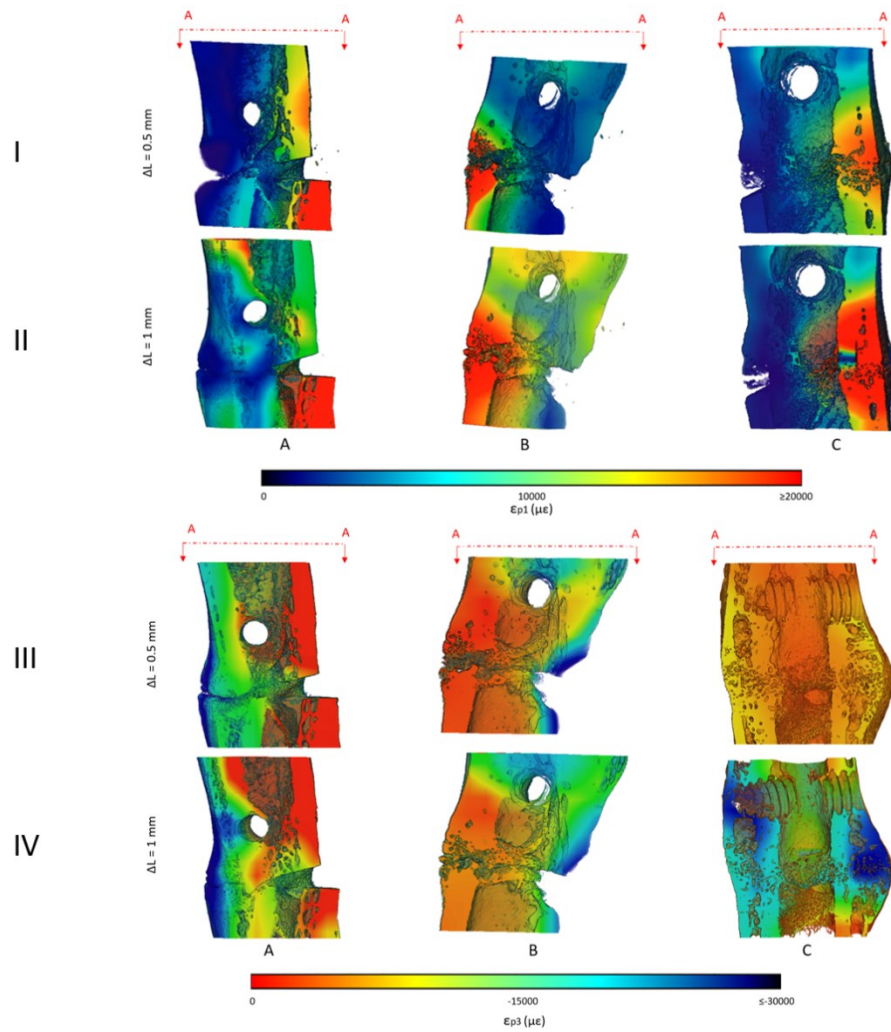


Figure 4. DVC analysis of 1 mm osteotomy gap, showing ϵ_{p1} and ϵ_{p3} of cross sections (A-A) in the ROIs of S2 (A), S3 (B) and S4 (C) in the first and second compression steps (I and II for ϵ_{p1} ; III and IV for ϵ_{p3} , respectively).

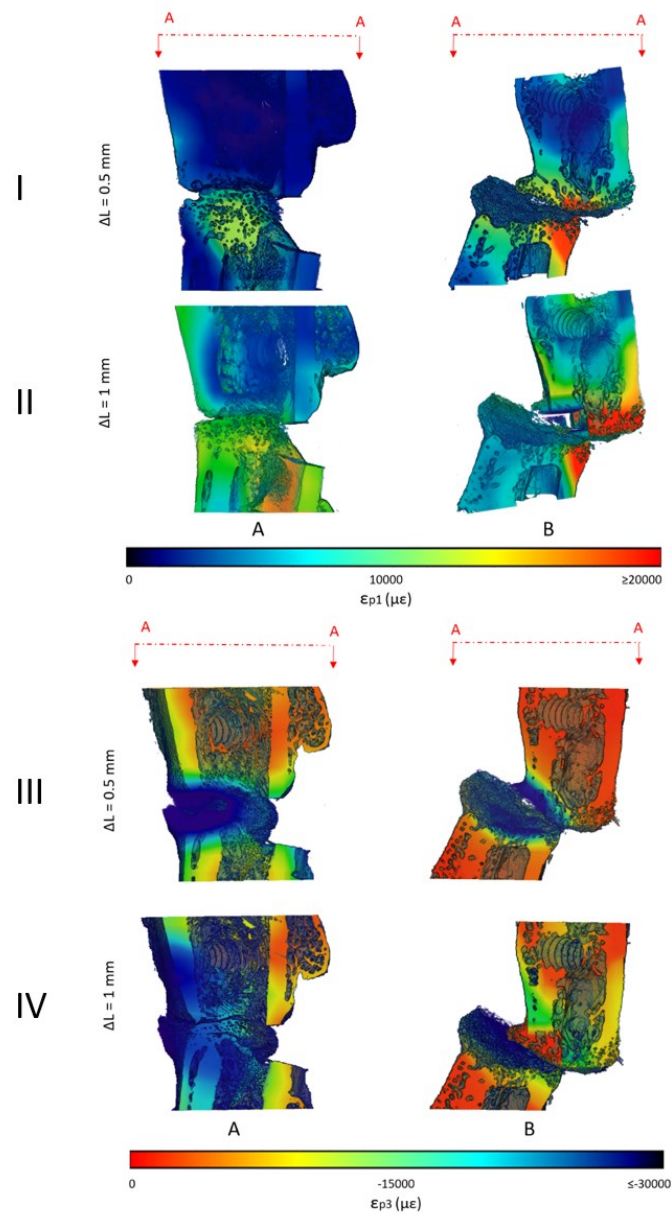


Figure 5. DVC analysis of 2 mm osteotomy gap, showing ϵ_{p1} and ϵ_{p3} of cross sections (A-A) in the ROIs of S5 (A) and S6 (B) in the first and second compression step (I and II for ϵ_{p1} ; III and IV for ϵ_{p3} , respectively).

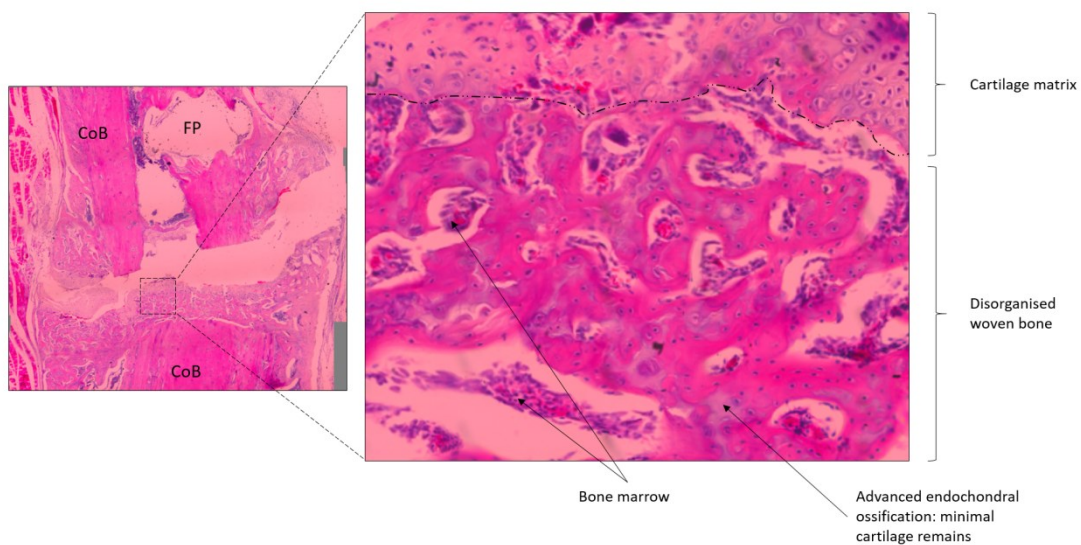


Figure 6. Histology images of fracture healing in progress of 1 mm osteotomy gap (S3). Images shown at x10 and x50 magnification; CoB: cortical bone, FP: fixator pin location.

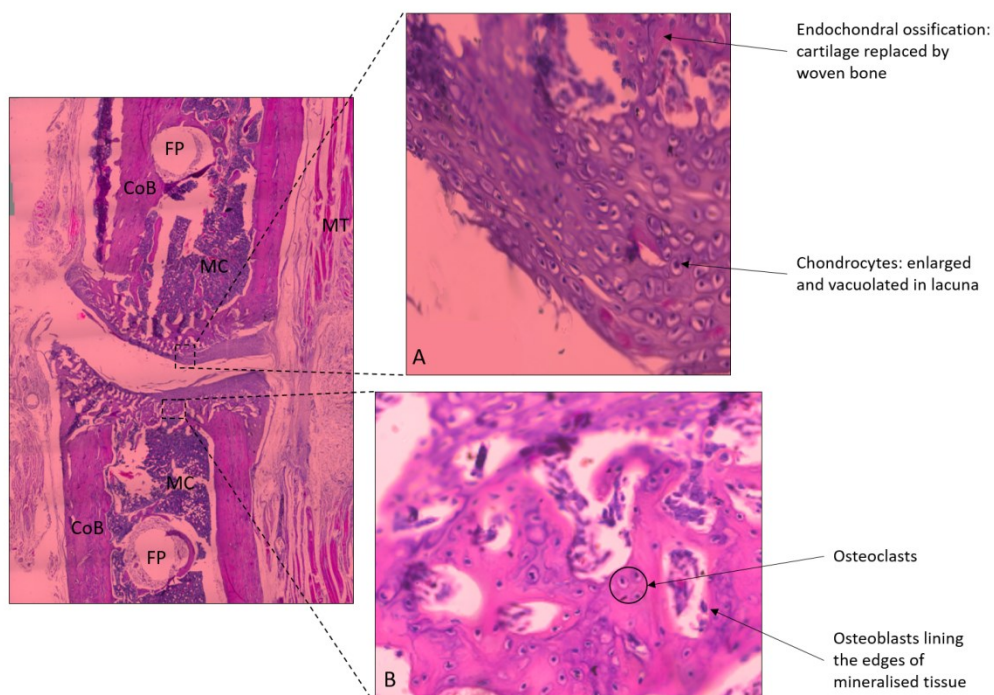


Figure 7. Histology images of pseudarthrosis of 2 mm osteotomy gap (S6). Images shown at x10 and x50 magnification; MT: muscular tissue, MC: marrow cavity, CoB: cortical bone, FP: fixator pin location. (A): Cartilage matrix, (B): region of endochondral ossification.